ACS APPLIED MATERIALS & INTERFACES

Research Article

Cite This: ACS Appl. Mater. Interfaces 2019, 11, 34408−34415

www.acsami.org

Variation of Interfacial Interactions in $PC_{61}BM$-like Electron-Transporting Compounds for Perovskite Solar Cells

Olivia Fernandez-Delgado,[†,¶] Edison Castro,[†,‡,¶] Carolina R. Ganivet,[†] Kaylin Fosnacht,[†,§] Fang Liu,[∥] Tom Mates,[⊥] Ying Liu,[#] Xiaojun Wu,[#] and Luis Echegoyen*[,†]

[†]Department of Chemistry and Biochemistry, University of Texas at El Paso, 500 West University Avenue, El Paso, Texas 79968, United States

[‡]Department of Chemistry, University of Pittsburgh, Pittsburgh, Pennsylvania 15260, United States

[§]Department of Natural Sciences, Saint Martin's University, Lacey Washington 98503-7500, United States

[∥]Department of Chemistry, Columbia University, New York, New York, 10027, United States

[⊥]Materials Department, University of California in Santa Barbara, California 93106-5050, United States

[#]Hefei National Lab for Physical Sciences at the Microscale, School of Chemistry and Material Sciences, and CAS Key Laboratory of Materials for Energy Conversion, University of Science and Technology of China, Hefei, Anhui 230026, China

Supporting Information

ABSTRACT: The synthesis, characterization, and incorporation of phenyl-C_{61}-butyric acid methyl ester ($PC_{61}BM$)-like derivatives as electron transporting materials (ETMs) in inverted perovskite solar cells (PSCs) are reported. These compounds have the same structure except for the ester substituent, which was varied from methyl to phenyl to thienyl and to pyridyl. The three latter derivatives performed better than $PC_{61}BM$ in PSCs, mainly attributed to the specific interactions of the fullerenes with the perovskite layer, as evidenced by X-ray photoelectron spectroscopy (XPS) and steady-state and time-resolved photoluminescence (SS- and TRPL) measurements. The experimental results were fully supported by density functional theory (DFT) calculations, which showed that the strongest interactions were exhibited by the compound possessing the pyridyl substituent.

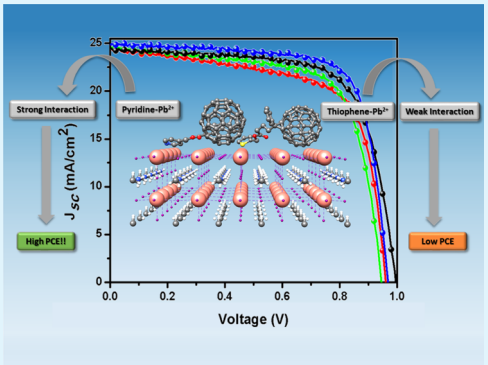

KEYWORDS: *fullerene derivatives, thiophene, pyridine, electron transporting materials, perovskite solar cells, interfacial interactions*

INTRODUCTION

With the world's increasing energy consumption and the growing concerns about the widespread use of fossil fuels, a search for alternative, renewable energy sources is underway, with solar power being one of the most promising alternatives. Perovskite solar cells (PSCs) are a relatively new type of solar cells that have become a hot topic of research starting in 2009.[1] Since then, solar cell performance has quickly improved, from 3.8[1] to 23.7%[2] in 2019. Their fast production, ease of fabrication, and the immense possibilities in terms of tunability of the materials make PSCs one of the best candidates for harvesting solar energy. Although PSCs have many advantages due to their high absorption in the UV−vis range,[1,3,4] their stability is limited, and it is highly dependent on the operation conditions. PSCs have been shown to degrade under continuous illumination[5−9] in the presence of water or high humidity conditions[10] as well as in the presence of oxygen.[9,11,12] These drawbacks have motivated the scientific community to find alternatives to improve the stability of PSCs[13] under normal, atmospheric conditions.[8,14] One way is to modify the perovskite layer by introducing mixed metal cations and anions to improve the lattice stability;[15,16] or by the addition of organic compounds,[17−20] polymers[18,21,22] and salts.[23] Another way to improve perovskite stability is by passivation of the grain boundaries, either with hydrophobic molecules or with compounds that assist with electron or hole extraction.[9,24,25] In this context, fullerenes have played an important role due to their ability to extract and transport electrons from the perovskite to the electrodes.[14] The most commonly used fullerene derivative as the electron transporting material (ETM) is $PC_{61}BM$ because of its high electron mobility and crystalline packing which allows efficient electron transport through the bulk layer.[26] It has been reported that fullerene derivatives with enhanced solubilities can effectively passivate the grain boundaries of the perovskite layer, thus decreasing the charge density on the surface and avoiding charge recombination,[27] ultimately resulting in improved photovoltaic performance. Recent work has focused on studying the specific interfacial interactions of the perovskite with the adjacent layers.[28−30] It has been reported

Received: May 28, 2019
Accepted: July 18, 2019
Published: July 18, 2019

DOI: 10.1021/acsami.9b09018
ACS Appl. Mater. Interfaces 2019, 11, 34408−34415

Scheme 1. Synthesis of $PC_{61}BPy$, $PC_{61}BTh$, and $PC_{61}BBz$

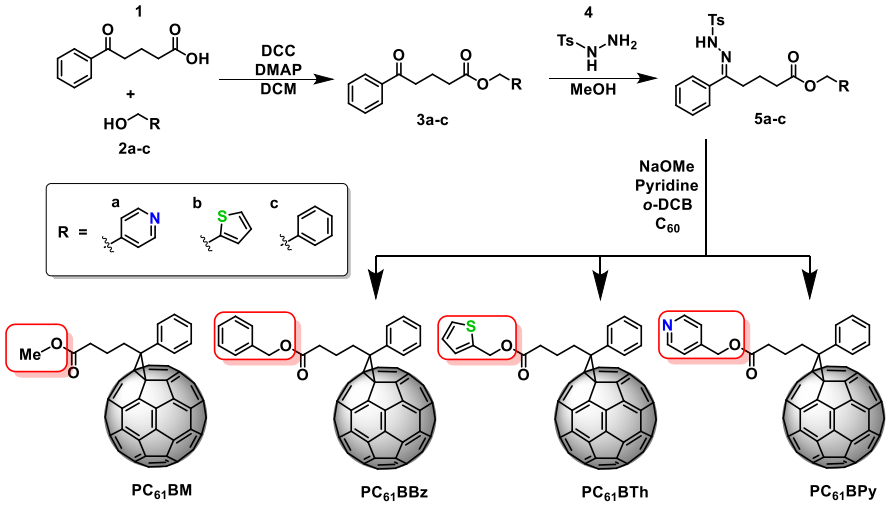

that functionalized fullerenes can exhibit effective interactions with the perovskite layer and lead to passivation of the latter.[31−34] In this work, we report the synthesis, characterization, and incorporation of $PC_{61}BM$-like derivatives with different ester groups to study the interfacial interactions of the addends with the perovskite layer, and the influence of such interactions on the photovoltaic performance. We systematically varied the structures to isolate the effects of the selected functional groups on device performances and interfacial interactions. The experimental results and conclusions were fully supported with density functional theory (DFT) calculations.

RESULTS AND DISCUSSION

The motivation for this work was to study the passivation and interfacial interaction effects between fullerene's ester substituents and the perovskite layer, as well as their photovoltaic performance. The $PC_{61}BM$-like derivatives ($PC_{61}BPy$, $PC_{61}BTh$, and $PC_{61}BBz$[35]) were synthesized as illustrated in Scheme 1, following a synthetic pathway developed by Hummelen et al.[36] The chemical structures of all compounds were confirmed by means of MALDI-TOF, ^1H NMR, ^{13}C NMR, and UV−vis absorption (see Supporting Information Figures S1−S3, respectively).

The electrochemical properties of all compounds were measured using cyclic voltammetry (CV). The measurements were recorded using a glassy carbon electrode in *o*-DCB solutions with 0.05 M *n*-Bu_4NPF_6 as the electrolyte. Very similar reduction potentials were observed for $PC_{61}BM$,[37] $PC_{61}BBz$, $PC_{61}BTh$, and $PC_{61}BPy$, which showed at least two well-defined and quasireversible redox waves (Figure S4a−d).

The lowest unoccupied molecular orbital (LUMO) energy levels of all derivatives were calculated from their onset reduction potentials (E^{on}_{red}) using eq 1.[38] The LUMO values are summarized in Table 1. The HOMO energy levels of the fullerene derivatives were calculated from their UV−vis absorption onset (E_g) (Figure S3) using eq 2.

Not surprisingly, the results show that the HOMO/LUMO values of $PC_{61}BM$, $PC_{61}BBz$, $PC_{61}BTh$, and $PC_{61}BPy$ are not substantially affected by the presence of the ester groups (Table 1) and thus they should all be effective as ETMs in PSCs (Figure 1).

Table 1. Optical Band gap, First Reduction Onset, and HOMO/LUMO Energy Levels of $PC_{61}BM$, $PC_{61}BBz$, $PC_{61}BTh$, and $PC_{61}BPy$

compound	λ_{abs} (nm)	E_g (eV)	E^{on}_{red} (V)	LUMO (eV)	HOMO (eV)
$PC_{61}BM$	718	1.73	−0.90	−3.99	−5.65
$PC_{61}BBz$	710	1.75	−1.00	−3.80	−5.60
$PC_{61}BTh$	710	1.75	−1.08	−3.72	−5.51
$PC_{61}BPy$	710	1.75	−1.09	−3.71	−5.40

$$\text{LUMO} = -e(E^{on}_{red} + 4.8)(\text{eV}) \quad (1)$$

$$E_g = 1242/\lambda_{onset} \quad (2)$$

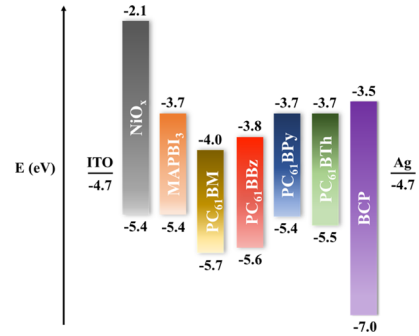

Figure 1. Schematic illustration of the estimated HOMO and LUMO energy levels, calculated from CV and UV−vis absorption.

To test the electron transport ability of the fullerenes, electron-only devices with an architecture of indium tin oxide (ITO)/Ag/fullerene/Ag were fabricated. The measurements were recorded under dark ambient conditions using the space-charge-limited current method.[39] The values obtained were 3.82×10^{-4}, 3.70×10^{-4}, 3.65×10^{-4}, and 3.66×10^{-4} $cm^2 \cdot V^{-1} \cdot s^{-1}$ for $PC_{61}BM$, $PC_{61}BBz$, $PC_{61}BTh$, and $PC_{61}BPy$, respectively. All derivatives display very similar electron mobility (μ_e) values, supporting their use as ETMs in PSCs (Figure S5a−d). These results clearly exclude the influence of the ester substituents in energy levels and electron mobility and confirm that the evaluation of the device performance is largely based on the interfacial interaction between the fullerene and the perovskite layer.

DOI: 10.1021/acsami.9b09018
ACS Appl. Mater. Interfaces 2019, 11, 34408−34415

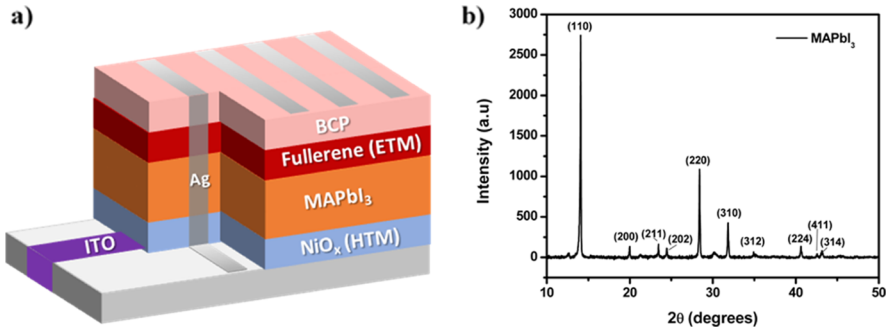

Figure 2. (a) PSC device architecture; (b) XRD of the perovskite film.

PSCs with an ITO/NiO_x/$CH_3NH_3PbI_3$/ETM/BCP/Ag configuration were fabricated (Figure 2a) to study the ability of PC_{61}BBz, PC_{61}BTh, and PC_{61}BPy to work as ETMs. The perovskite layer was characterized by X-ray diffraction (XRD). As shown in Figure 2b, it presents a very predominant peak at 14° for the 110 facet. The intensity of these peaks indicates a high level of crystallinity. Other distinctive peaks for the tetragonal phase were observed for the 200, 211, 202, 220, 310, 312, 224, 411, and 314 planes at 20°, 24°, 25°, 28°, 32°, 35°, 41°, 42°, and 43°, respectively.

The perovskite layer was also characterized by scanning electron microscopy (SEM). Figure 3 shows the surface (a) and cross-section SEM (b). As shown in Figure 3a, a crystalline and homogeneous layer was obtained, with an average grain size of 200 nm. In Figure 3b, all layers of the device are visible, starting with the ITO (150 nm), NiO_x (50 nm), $MAPbI_3$ (350 nm), fullerene (100 nm), and bathocuproine (BCP) (30 nm). The thicknesses of the different layers were optimized and measured not only by SEM but also with surface profilometry and exhibited very high reproducibility.

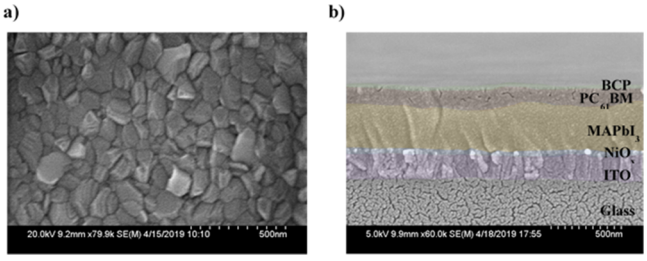

Figure 3. (a) Top-view SEM and (b) cross-section SEM.

The current−voltage J−V curves for the fabricated PSCs are shown in Figure 4a. Devices based on PC_{61}BM as the ETM were used as the control, and these exhibited an average power conversion efficiency (PCE) value of 15.97%, an open circuit voltage (V_{oc}) of 0.965 V, a fill factor (FF) of 72%, and a short circuit current (J_{sc}) of 23.1 mA/cm^2. The PSCs performances are summarized in Table 2. A statistical study of the PCEs was performed (Figure S6) to test the devices' reproducibility, and PC_{61}BM-based devices exhibited the smallest errors (Table 2) being the others acceptable.

When PC_{61}BBz, PC_{61}BTh, and PC_{61}BPy were used as the ETMs, the PCE values were all higher, and the best performances were observed for PC_{61}BPy-based devices. These enhanced PCEs are likely the result of the specific interactions between the heteroatoms from the ester substituents (nitrogen and sulfur) with Pb^{2+} in the perovskite layer. These Lewis acid−base interactions in which the S and the N donate a pair of electrons to Pb^{2+} can establish an effective interfacial connection between the two layers and passivate the surface, thus eliminating the trap sites in the perovskite layer.

To further investigate the nature of the interfacial interactions between the perovskite surface and the fullerene derivatives, X-ray photoelectron spectroscopy (XPS) measurements were performed (Figure 5). The results showed that PC_{61}BM, PC_{61}BBz, and PC_{61}BTh exhibited small shifts of the Pb 4f electrons toward higher binding energy.

Interestingly, PC_{61}BPy showed a much larger $4f_{7/2}$ binding energy shift, from 138.4 to 139.2 eV. This pronounced change is likely the result of a very strong interaction between Pb^{2+} in the perovskite and the pyridine group. The 3d levels of I^- exhibited a smaller shift, attributed to the disruption of neighboring Pb^{2+}. Similar to the Pb orbital shifts, the I orbitals

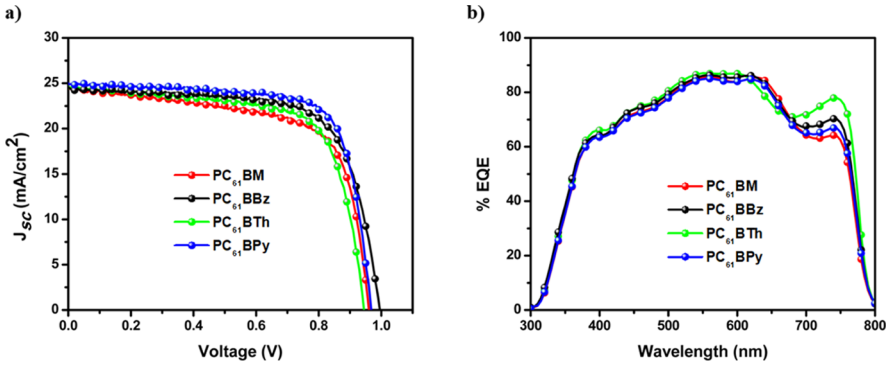

Figure 4. (a) J−V curves and (b) EQE characteristics of PC_{61}BM, PC_{61}BBz, PC_{61}BTh, and PC_{61}BPy-based devices.

DOI: 10.1021/acsami.9b09018
ACS Appl. Mater. Interfaces 2019, 11, 34408−34415

Table 2. Summary of the PSC Photovoltaic Performance Using $PC_{61}BM$, $PC_{61}BBz$, $PC_{61}BPy$, and $PC_{61}BTh$ as the ETMs

compound	J_{sc} (mA/cm^2)	J_{sc}[a] (mA/cm^2)	V_{oc} (V)	FF (%)	PCE (%)
$PC_{61}BM$	24.50 ± 0.16	23.2	0.962 ± 0.003	70 ± 3	15.72 ± 0.14 (15.97)
$PC_{61}BBz$	24.33 ± 0.22	23.9	0.999 ± 0.003	69 ± 1	16.57 ± 0.28 (16.92)
$PC_{61}BPy$	24.85 ± 0.06	24.1	0.966 ± 0.005	74 ± 1	17.46 ± 0.22 (17.84)
$PC_{61}BTh$	24.12 ± 0.19	23.5	0.950 ± 0.005	68 ± 1	15.74 ± 0.33 (16.07)

[a]Is the calculated current from the EQE measurements, and the values in parentheses are the highest values obtained.

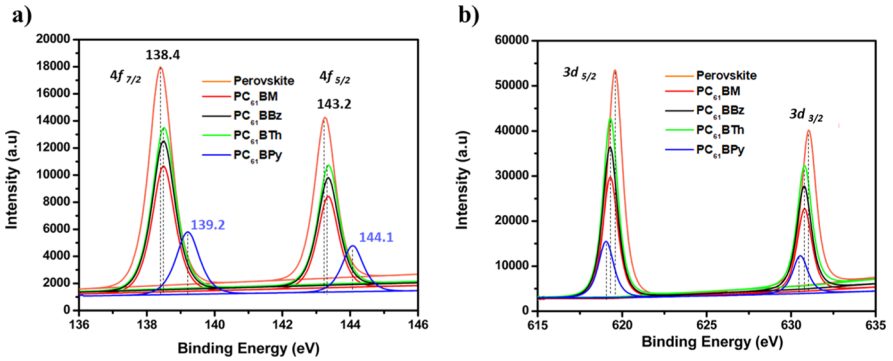

Figure 5. XPS measurements for (a) Pb orbitals and (b) I orbitals. The input X-ray source was aluminum k-alpha (1486 eV).

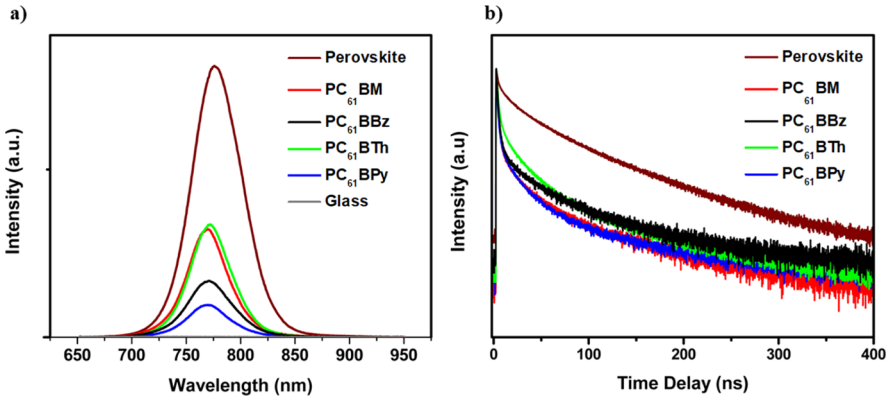

Figure 6. (a) SSPL and (b) TRPL of $MAPbI_3$ and $MAPbI_3$/fullerene films. The excitation wavelength was 405 nm, and the emission wavelength was 760 nm.

were shifted more by $PC_{61}BPy$. These results are perfectly consistent with the observed photovoltaic device performances.

Recently, some reports have shown that the presence of pyridine or other amine groups can improve the interactions with Pb^{2+}, as shown by XPS measurements, where clear changes in the binding energy were observed.[18,19,31,40,41]

The passivation abilities of the fullerene derivatives were tested using steady-state photoluminescence (SSPL) and time-resolved photoluminescence (TRPL) for devices containing $MAPbI_3$ and $MAPbI_3$/fullerene structures. In Figure 6a, a peak with high intensity can be observed for the emission resulting from electron/hole recombination for samples containing only the perovskite layer. When a fullerene derivative was deposited onto the perovskite layer, significant PL quenching was observed. The pronounced decrease of the signals in the presence of the fullerene derivatives shows that the charge trap sites and grain boundaries are being passivated by the fullerenes at the interfaces. Figure 6b shows the TRPL decay measurements, monitoring the emission peak of the different fullerene derivatives coated on the perovskite layers as a function of time. All devices showed two decay domains, fast and slow, described by τ_1 and τ_2, respectively, using a biexponential fitting procedure. The fast decay represents the carrier lifetime until its extraction by the ETM, while the slow decay is associated with the radiative decay.

As represented in Table 3, the perovskite layer exhibits the longest τ_1 at 19 ns. After the fullerenes were coated onto this layer, a reduction of τ_1 was observed, with values of 10.7, 10.0, 9.4, and 5.1 ns for $PC_{61}BTh$, $PC_{61}BM$, $PC_{61}BB$, and $PC_{61}BPy$, respectively. τ_1 is a measure of the extraction efficiency of the electrons from the perovskite surface, and $PC_{61}BPy$ exhibited the best extraction ability. The same trend was observed for τ_2 (Table 3). These results are in perfect agreement with the photovoltaic performance results and the XPS measurements.

Table 3. Carrier Lifetimes for $MAPbI_3$ and $MAPbI_3$/Fullerene Films

sample	perovskite	$PC_{61}BM$	$PC_{61}BBz$	$PC_{61}BTh$	$PC_{61}BPy$
τ_1/ns	19.0	10.0	9.4	10.7	5.1
τ_2/ns	1.4	1.2	1.2	1.3	0.7

DOI: 10.1021/acsami.9b09018
ACS Appl. Mater. Interfaces 2019, 11, 34408−34415

Stability studies were conducted for unencapsulated devices under ambient conditions and 50% humidity for 7 days (Figure S7). Overall, devices fabricated with all $PC_{61}BM$-like derivatives retained more than 79% of their initial PCE. A much higher stability was observed for $PC_{61}BPy$-based devices, which retained up to 92% of their initial PCE values and with no visual signs of degradation.

DFT Calculations. All calculations were carried out based on the DFT method with a generalized gradient approximation and Perdew–Burke–Ernzerhof exchange–correlation functional as implemented in the Vienna Ab initio Simulation Package. The van der Waals interactions were corrected via Grimme's semiempirical corrections (DFT-D3). A 2 × 2 supercell of the $CH_3NH_3PbI_3$ (110) surface (the predominant facet as reported earlier from XRD measurements of the perovskite film) with PbI_2 as the terminal was used, and the vacuum thickness was set to 20 Å. The atoms in the bottom layer were fixed at their bulk positions, while other atoms were relaxed. A plane-wave cutoff energy of 400 (450) eV and Γ point were used for structure optimization (self-consistent calculation). The convergence threshold for self-consistent iteration was set to 10^{-5} eV, and the unfixed atomic positions were fully optimized until the force on each atom was less than 0.05 eV/Å. The adsorption energies (E_{ads}, kJ/mol) for C_{60}–$CH_3NH_3PbI_3$ were calculated using $E_{ads} = E(C_{60}\text{-X@}CH_3NH_3PbI_3) - E(CH_3NH_3PbI_3) - E(C_{60}\text{-X})$, C_{60}-X = $PC_{61}BPy$, $PC_{61}BTh$, $PC_{61}BBz$, and $PC_{61}BM$, where $E_{(structure)}$ is the calculated energy of the corresponding structure.

First, the interaction of the fullerene cage with the perovskite surface was analyzed to determine the most stable configuration. To calculate this, C_{60} was positioned in the three main adsorption sites (Figure 7a–c). The adsorption energies were

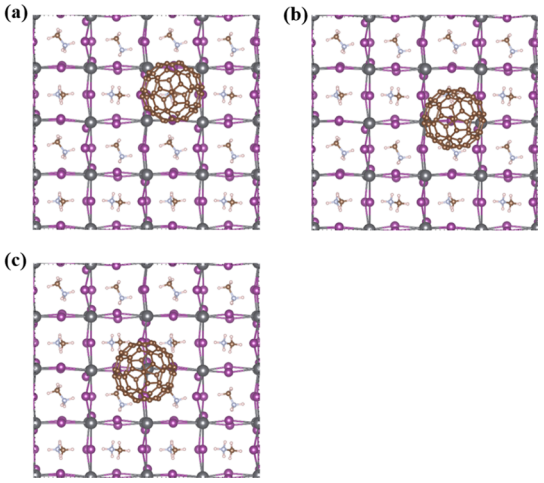

Figure 7. Top view of the possible adsorption sites for the C_{60} cage.

(a) −74.3, (b) −56.9, and (c) −70.4 kJ/mol, respectively, which means that the most favorable interaction is obtained when the C_{60} cage is in the adsorption site (a), and this was the position adopted during subsequent calculations. Then, the compounds were considered with the attached addends (Figure 8). The moieties can interact with the surface Pb^{2+} in two principal orientations via the carbonyl group oxygen or via the ester substituents (benzyl, thienyl, or pyridyl). These interactions are mutually exclusive because of the conformational changes in the alkyl chain that prevent the two groups from interacting simultaneously with the Pb^{2+} ions. The

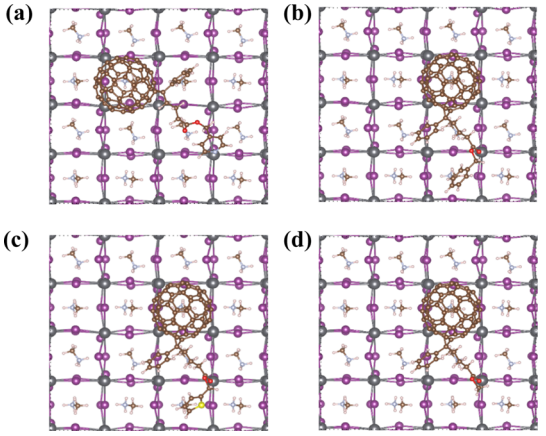

Figure 8. Top view of the adsorption structure of the fullerene derivatives on the $CH_3NH_3PbI_3$ (110) surface. (a) $PC_{61}BPy$, (b) $PC_{61}BBz$, (c) $PC_{61}BTh$, and (d) $PC_{61}BM$.

interactions via the carbonyl group oxygens were tested. In the case of $PC_{61}BM$, this is the principal interaction mode because it lacks an appropriate ester substituent to interact with the surface Pb^{2+}. The interactions via the ester substituents were then probed. All bond distances between the carbonyl group and Pb^{2+} as well as between the ester groups and Pb^{2+} are summarized in Table 4.

Table 4. Distance between Fullerene Derivatives and the $CH_3NH_3PbI_3$ Surface

compound	Pb–N (Å)	Pb–Bz (Å)	Pb–S (Å)	Pb–O=C (Å)
$PC_{61}BPy$	2.61			2.60
$PC_{61}BBz$		3.13		2.58
$PC_{61}BTh$			3.37	2.60
$PC_{61}BM$				2.63

In Table 5, all adsorption energies are displayed. Notice that the values include the interaction of the fullerene cage with the

Table 5. Adsorption Energies between Fullerene Derivatives and the $CH_3NH_3PbI_3$ Surface

compound	Pb–N (kJ/mol)	Pb–Bz (kJ/mol)	Pb–S (kJ/mol)	Pb–O=C (kJ/mol)
$PC_{61}BPy$	−199.6			−168.8
$PC_{61}BBz$		−156.3		−173.7
$PC_{61}BTh$			−148.6	−170.8
$PC_{61}BM$				−155.3

surface of the perovskite as well as the interaction of the addends with the Pb^{2+} ions. According to the results, $PC_{61}BPy$ has exhibited the strongest interaction via the N of the pyridine with the surface Pb^{2+} with an adsorption energy of −199.7 kJ/mol and a Pb–N bond length of 2.61 Å. The interaction of $PC_{61}BPy$ via carbonyl oxygen is much weaker. The rest of the derivatives exhibited a stronger interaction between the oxygen on the carbonyl group and Pb^{2+}, being −173.7, −170.8, and −155.3 kJ/mol for $PC_{61}BBz$, $PC_{61}BTh$, and $PC_{61}BM$, respectively. These results support the experimental data obtained by XPS as well as the photovoltaic performances observed for the corresponding devices with the different derivatives.

DOI: 10.1021/acsami.9b09018
ACS Appl. Mater. Interfaces 2019, 11, 34408–34415

The differential charge density map shows that electron charge is mainly localized on the functional groups in the fullerene derivatives when adsorbed on the perovskite layer as shown in Figure 9.

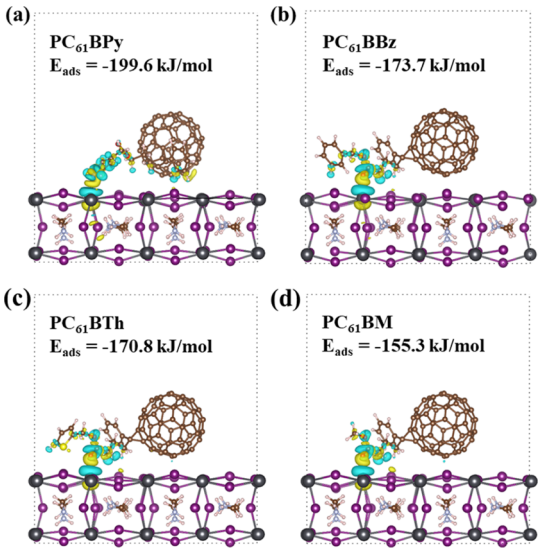

Figure 9. Differential charge density map of the fullerene derivatives adsorbed on the $CH_3NH_3PbI_3$ (110) surface; isosurfaces are set to 0.001, and the labeled E_{ads} in the figure indicates the adsorption energy.

CONCLUSIONS

In this work, we synthesized and characterized three $PC_{61}BM$-like fullerene derivatives and evaluated them in p-i-n-inverted PSCs as ETMs. The compounds were systematically designed so that only the ester residue was changed to probe the influence on photovoltaic performance and interfacial interactions. The results showed a significant improvement of the PCE when these derivatives were used compared to the control devices based on $PC_{61}BM$. The pyridine group exhibited a clear and strong interaction with Pb^{2+} on the surface of the perovskites as indicated by XPS, SSPL, and TRPL results. These interactions lead to substantial photovoltaic performance improvements. The thiophene group did not exhibit a strong interaction with the perovskite, as reflected by a lower performance and decreased ability to passivate the devices based on this derivative. The perovskite passivation ability of these derivatives was evidenced by SSPL and TRPL. Finally, DFT calculations were also performed to explain the nature of the fullerene−perovskite interactions. Our results showed that the pyridine group in $PC_{61}BPy$ enhances the interfacial interactions with the Pb ions on the perovskite surface, which leads to higher charge trap passivation and to a consequent decrease of electron/hole recombination. The rest of the derivatives, $PC_{61}BBz$, $PC_{61}BTh$, and $PC_{61}BM$ have a preferred interaction via the carbonyl group oxygen with the surface Pb rather than with ester substituent. The computational results completely agree with the experimental findings and support the idea that pyridine-based fullerene derivatives could lead to further performance enhancement for PSCs.

EXPERIMENTAL SECTION

Materials Synthesis. All chemicals were of reagent grade. Silica gel (40−60 μ, 60 Å) was used to separate and purify the products. Matrix-assisted laser desorption/ionization time-of-flight mass spectroscopy (MALDI-TOF-MS) was conducted on the positive mode, with samples dissolved in chloroform and 1,1,4,4-tetraphenyl-1,3-butadiene as the matrix. NMR spectra were recorded using a Bruker 400 MHz spectrometer. The UV/vis−NIR spectra were recorded for chloroform solutions. CV experiments were carried out under an argon atmosphere at room temperature. The scan rate for the CV experiments was 100 mV/s. A one compartment cell with a standard three-electrode setup was used, consisting of a 1 mm diameter glassy carbon disk as the working electrode, a platinum wire as the counter electrode, and a silver wire as a pseudo-reference electrode, in a solution of anhydrous *ortho*-dichlorobenzene (*o*-DCB) containing 0.05 M n-Bu_4NPF_6. Ferrocene was added to the solution at the end of each experiment as an internal standard.

General Synthesis of 5-Oxo-5-phenylpentanoate Derivatives (3a−c). In a two-neck round-bottom flask equipped with a magnetic stirrer, 5-oxo-5-phenylpentanoic acid (**1**), alcohol (**2a−c**), *N*,*N*′-dicyclohexylcarbodiimide, and dimethylaminopyridine were mixed together in dichloromethane (50 mL) at 0 °C. The mixture was degassed with Ar for 10 min and stirred for 12 h at room temperature. After this time, the reaction was filtered, and the solvent was removed under reduced pressure. The resulting product was chromatographed using silica gel and a mixture of ethyl acetate and hexanes (3:1).

General Synthesis of the 5-Phenyl-5-(2-tosylhydrazono)-pentanoate Derivatives (5a−c). To a two-neck round-bottom flask were added **3a−c** and *p*-toluenesulfonyl hydrazide (**4**) followed by 15 mL of anhydrous MeOH. The reaction was stirred for 18 h under reflux and allowed to cool down to room temperature, and the resulting precipitate was filtered and washed with cold MeOH. The resulting solid was chromatographed using silica gel and a mixture of ethyl acetate and hexanes (3:1).

General Synthesis of Phenyl-C_{61}-Butyric Acid Methyl Ester Derivatives ($PC_{61}BBz$, $PC_{61}BTh$, and $PC_{61}BPy$). A mixture of **5a−c**, sodium methoxide, and dry pyridine (5.0 mL) was placed under a nitrogen atmosphere and stirred for 30 min at room temperature. A solution of C_{60} in 15 mL of *o*-DCB was added and refluxed overnight. The solvent was removed under vacuum, and the crude product was purified by chromatography on silica gel using toluene as the eluant (to separate the unreacted C_{60}), followed by chloroform to collect the final products.

Device Fabrication. ITO-coated glass was purchased from Liaoning Huite Photoelectric Technology Co., Ltd. $PC_{61}BM$ (99%) was bought from SES Research. Methylammonium iodide (CH_3NH_3I, 99.5%) was bought from Greatcellsolar. PbI_2 (99%) was bought from Sigma-Aldrich. The configuration used for the fabrication of the PSCs was Glass/ITO/NiO_x/$CH_3NH_3PbI_3$/ETM/BCP/Ag. The patterned ITO glass substrates were cleaned sequentially with detergent, deionized water, isopropanol, and acetone, each step for 30 min, dried with nitrogen gas, and finally treated with UV−ozone for 30 min. A solution of 25 mg of nickel acetate dihydrate in 1 mL of ethanol was prepared and stirred overnight. The resulting blue solution was deposited onto the treated ITO substrates at 3000 rpm for 40 s and heated at 350 °C for 30 min in air. The substrates were then transferred to a N_2-filled glovebox, where $CH_3NH_3PbI_3$ (1.2 M solution in DMF/DMSO, 7:3) was spin-coated on top of the NiO_x-coated substrates at 1000 rpm for 5 s and at 6000 rpm for 45 s. Toluene (500 μL) was added 10 s after the second step, and then, the devices were annealed at 100 °C for 10 min. The fullerene derivatives dissolved in chlorobenzene (20 mg/mL) were spin-coated onto the $CH_3NH_3PbI_3$ layer at 1000 rpm for 60 s and annealed at 80 °C for 15 min. Then, a solution of 1 mg/mL of BCP in ethanol was spun onto the fullerene layer at 4000 rpm for 30 s. Finally, Ag electrodes (100 nm) were deposited by thermal evaporation under a pressure of 1×10^{-6} Torr through a shadow mask. The active area of the fabricated devices was 6 mm^2.

Device Characterization. Current−Voltage (J−V) characteristics of the devices were tested using a Keithley 2420 source meter under a Photo Emission Tech SS100 Solar Simulator, and the light intensity was calibrated by a standard Si solar cell. External quantum

DOI: 10.1021/acsami.9b09018
ACS Appl. Mater. Interfaces 2019, 11, 34408−34415

efficiencies (EQE) were measured using a Bentham (from Bentham Instruments Ltd) measurement system. The light intensity was calibrated using a single-crystal Si photovoltaic cell as the reference. The $J-V$ and EQE measurements were obtained in air. The SEM images were collected using a ZEISS Sigma field-emission scanning electron microscopy, where the electron beam was accelerated in the range of 500 V to 30 kV. Film thicknesses were measured using a KLA Tencor profilometer. The steady-state PL spectra were recorded on a Horiba Yvon Nanolog spectrometer coupled with a time-correlated single-photon counting with nanoLED excitation sources for time-resolved emission measurements. XPS measurements were performed using a Kratos Axis Ultra DLD system. Survey and high-resolution spectra were run at pass energies of 160 and 20 eV, respectively. The energy scale was calibrated by adjusting aliphatic C 1s to 285.0 eV.

■ ASSOCIATED CONTENT

Supporting Information

The Supporting Information is available free of charge on the ACS Publications website at DOI: 10.1021/acsami.9b09018.

Experimental details about PL, TRPL, and XPS, detailed synthesis and characterization of the new derivatives by MALDI-TOF, ^{1}H and ^{13}C NMR, UV−vis, CV, and stability studies, and statistics and electron mobility measurements for the constructed devices (PDF)

■ AUTHOR INFORMATION

Corresponding Author

*E-mail: echegoyen@utep.edu.

ORCID

Olivia Fernandez-Delgado: 0000-0002-6641-026X

Edison Castro: 0000-0003-2954-9462

Xiaojun Wu: 0000-0003-3606-1211

Luis Echegoyen: 0000-0003-1107-9423

Author Contributions

¶O.F.-D and E.C. contributed equally.

Notes

The authors declare no competing financial interest.

■ ACKNOWLEDGMENTS

The authors thank the US National Science Foundation (NSF) for generous support of this work under the NSF-PREM program (DMR 1205302), CHE-1408865 (to L.E.), and 1401188 (to F. D.). The Robert A. Welch Foundation is also gratefully acknowledged for an endowed chair to L. E. (grant AH-0033). For use of the UCSB MRSEC XPS facility, we also acknowledge support from the National Science Foundation under grant number DMR-1720256. This research was also supported in part by the Department of Energy (DOE) Office of Energy Efficiency and Renewable Energy (EERE) Postdoctoral Research Award under the EERE Solar Energy Technologies Office administered by the Oak Ridge Institute for Science and Education (ORISE) for the DOE. ORISE is managed by Oak Ridge Associated Universities (ORAU) under DOE contract number DE-SC00014664. X.W. is supported by the National Key Research and Development Program of China (2016YFA0200602, 2018YFA0208603), NSFC (21573204, 21421063), the Anhui Initiative in Quantum Information Technologies, and the Fundamental Research Funds for the Central Universities. All opinions expressed in this paper are the authors' and do not necessarily reflect the policies and views of DOE, ORAU, or ORISE. The authors would also like to thank Prof. X−Y Zhu and his research group for his help with SSPL and TRPL measurements and Dr. Metta for his help with XRD measurements.

■ REFERENCES

(1) Kojima, A.; Teshima, K.; Shirai, Y.; Miyasaka, T. Organometal Halide Perovskites as Visible-Light Sensitizers for Photovoltaic Cells. *J. Am. Chem. Soc.* **2009**, *131*, 6050−6051.

(2) NREL Best Research-Cell Efficiencies. https://www.nrel.gov/pv/assets/pdfs/best-reserch-cell-efficiencies.pdf (accessed March, 2019).

(3) Cao, D. H.; Stoumpos, C. C.; Farha, O. K.; Hupp, J. T.; Kanatzidis, M. G. 2D Homologous Perovskites as Light-Absorbing Materials for Solar Cell Applications. *J. Am. Chem. Soc.* **2015**, *137*, 7843−7850.

(4) Grätzel, M. The Light and Shade of Perovskite Solar Cells. *Nat. Mater.* **2014**, *13*, 838−842.

(5) Kim, H.-S.; Lee, C.-R.; Im, J.-H.; Lee, K.-B.; Moehl, T.; Marchioro, A.; Moon, S.-J.; Humphry-Baker, R.; Yum, J.-H.; Moser, J. E.; Grätzel, M.; Park, N.-G. Lead iodide perovskite sensitized all-solid-state submicron thin film mesoscopic solar cell with efficiency exceeding 9%. *Sci. Rep.* **2012**, *2*, 591.

(6) Misra, R. K.; Aharon, S.; Li, B.; Mogilyansky, D.; Visoly-Fisher, I.; Etgar, L.; Katz, E. A. Temperature- and Component-Dependent Degradation of Perovskite Photovoltaic Materials under Concentrated Sunlight. *J. Phys. Chem. Lett.* **2015**, *6*, 326−330.

(7) O'Mahony, F. T. F.; Lee, Y. H.; Jellett, C.; Dmitrov, S.; Bryant, D. T. J.; Durrant, J. R.; O'Regan, B. C.; Graetzel, M.; Nazeeruddin, M. K.; Haque, S. A. Improved environmental stability of organic lead trihalide perovskite-based photoactive-layers in the presence of mesoporous TiO2. *J. Mater. Chem. A* **2015**, *3*, 7219−7223.

(8) Asghar, M. I.; Zhang, J.; Wang, H.; Lund, P. D. Device stability of perovskite solar cells - A review. *Renewable Sustainable Energy Rev.* **2017**, *77*, 131−146.

(9) Aristidou, N.; Sanchez-Molina, I.; Chotchuangchutchaval, T.; Brown, M.; Martinez, L.; Rath, T.; Haque, S. A. The Role of Oxygen in the Degradation of Methylammonium Lead Trihalide Perovskite Photoactive Layers. *Angew. Chem., Int. Ed.* **2015**, *54*, 8208−8212.

(10) Leguy, A. M. A.; Hu, Y.; Campoy-Quiles, M.; Alonso, M. I.; Weber, O. J.; Azarhoosh, P.; van Schilfgaarde, M.; Weller, M. T.; Bein, T.; Nelson, J.; Docampo, P.; Barnes, P. R. F. Reversible Hydration of $CH_3NH_3PbI_3$ in Films, Single Crystals, and Solar Cells. *Chem. Mater.* **2015**, *27*, 3397−3407.

(11) Yang, J.; Siempelkamp, B. D.; Liu, D.; Kelly, T. L. Investigation of $CH_3NH_3PbI_3$ Degradation Rates and Mechanisms in Controlled Humidity Environments Using in Situ Techniques. *ACS Nano* **2015**, *9*, 1955−1963.

(12) Christians, J. A.; Miranda Herrera, P. A.; Kamat, P. V. Transformation of the Excited State and Photovoltaic Efficiency of $CH_3NH_3PbI_3$ Perovskite upon Controlled Exposure to Humidified Air. *J. Am. Chem. Soc.* **2015**, *137*, 1530−1538.

(13) Collavini, S.; Saliba, M.; Tress, W. R.; Holzhey, P. J.; Völker, S. F.; Domanski, K.; Turren-Cruz, S. H.; Ummadisingu, A.; Zakeeruddin, S. M.; Hagfeldt, A.; Grätzel, M.; Delgado, J. L. Poly(ethylene glycol)-[60]Fullerene-Based Materials for Perovskite Solar Cells with Improved Moisture Resistance and Reduced Hysteresis. *Chemsuschem* **2018**, *11*, 1032−1039.

(14) Castro, E.; Murillo, J.; Fernandez-Delgado, O.; Echegoyen, L. Progress in Fullerene-based Hybrid Perovskite Solar Cells. *J. Mater. Chem. C* **2018**, *6*, 2635−2651.

(15) Noh, J. H.; Im, S. H.; Heo, J. H.; Mandal, T. N.; Seok, S. I. Chemical Management for Colorful, Efficient, and Stable Inorganic-Organic Hybrid Nanostructured Solar Cells. *Nano Lett.* **2013**, *13*, 1764−1769.

(16) Li, N.; Zhu, Z.; Chueh, C.-C.; Liu, H.; Peng, B.; Petrone, A.; Li, X.; Wang, L.; Jen, A. K.-Y. Mixed Cation FAxPEA1-xPbI3with Enhanced Phase and Ambient Stability toward High-Performance Perovskite Solar Cells. *Adv. Energy Mater.* **2017**, *7*, 1601307−9.

(17) Liang, C.; Zhao, D.; Li, P.; Wu, B.; Gu, H.; Zhang, J.; Goh, T. W.; Chen, S.; Chen, Y.; Sha, Z.; Shao, G.; Sum, T. C.; Xing, G.

Simultaneously Boost Diffusion Length and Stability of Perovskite for High Performance Solar Cells. *Nano Energy* **2019**, *59*, 721−729.
(18) Huang, Z.; Hu, X.; Liu, C.; Tan, L.; Chen, Y. Nucleation and Crystallization Control via Polyurethane to Enhance the Bendability of Perovskite Solar Cells with Excellent Device Performance. *Adv. Funct. Mater.* **2017**, *27*, 1703061.
(19) Lee, J.-W.; Kim, H.-S.; Park, N.-G. Lewis Acid-Base Adduct Approach for High Efficiency Perovskite Solar Cells. *Acc. Chem. Res.* **2016**, *49*, 311−319.
(20) Sandoval-Torrientes, R.; Pascual, J.; García-Benito, I.; Collavini, S.; Kosta, I.; Tena-Zaera, R.; Martín, N.; Delgado, J. L. Modified Fullerenes for Efficient Electron Transport Layer-Free Perovskite/Fullerene Blend-Based Solar Cells. *Chemsuschem* **2017**, *10*, 2023−2029.
(21) Fairfield, D. J.; Sai, H.; Narayanan, A.; Passarelli, J. V.; Chen, M.; Palasz, J.; Palmer, L. C.; Wasielewski, M. R.; Stupp, S. I. Structure and chemical stability in perovskite-polymer hybrid photovoltaic materials. *J. Mater. Chem. A* **2019**, *7*, 1687−1699.
(22) Zuo, L.; Guo, H.; deQuilettes, D. W.; Jariwala, S.; De Marco, N.; Dong, S.; DeBlock, R.; Ginger, D. S.; Dunn, B.; Wang, M.; Yang, Y. Polymer-modified Halide Perovskite Films for Efficient and Stable Planar Heterojunction Solar Cells. *Sci. Adv.* **2017**, *3*, No. e1700106.
(23) Zheng, H.; Liu, G.; Zhu, L.; Ye, J.; Zhang, X.; Alsaedi, A.; Hayat, T.; Pan, X.; Dai, S. The Effect of Hydrophobicity of Ammonium Salts on Stability of Quasi-2D Perovskite Materials in Moist Condition. *Adv. Energy Mater.* **2018**, *8*, 1800051.
(24) Stranks, S. D.; Eperon, G. E.; Grancini, G.; Menelaou, C.; Alcocer, M. J. P.; Leijtens, T.; Herz, L. M.; Petrozza, A.; Snaith, H. J. Electron-Hole Diffusion Lengths Exceeding 1 Micrometer in an Organometal Trihalide Perovskite Absorber. *Science* **2013**, *342*, 341−344.
(25) Bryant, D.; Aristidou, N.; Pont, S.; Sanchez-Molina, I.; Chotchunangatchaval, T.; Wheeler, S.; Durrant, J. R.; Haque, S. A. Light and Oxygen Induced Degradation Limits the Operational Stability of Methylammonium Lead Triiodide Perovskite Solar Cells. *Energy Environ. Sci.* **2016**, *9*, 1655−1660.
(26) Fang, Y.; Bi, C.; Wang, D.; Huang, J. The Functions of Fullerenes in Hybrid Perovskite Solar Cells. *ACS Energy Lett.* **2017**, *2*, 782−794.
(27) Tian, C.; Kochiss, K.; Castro, E.; Betancourt-Solis, G.; Han, H.; Echegoyen, L. A Dimeric Fullerene Derivative for Efficient Inverted Planar Perovskite Solar Cells with Improved Stability. *J. Mater. Chem. A* **2017**, *5*, 7326−7332.
(28) Yang, D.; Zhang, X.; Wang, K.; Wu, C.; Yang, R.; Hou, Y.; Jiang, Y.; Liu, S.; Priya, S. Stable Efficiency Exceeding 20.6% for Inverted Perovskite Solar Cells through Polymer-Optimized PCBM Electron-Transport Layers. *Nano Lett.* **2019**, *19*, 3313−3320.
(29) Cho, A.-N.; Park, N.-G. Impact of Interfacial Layers in Perovskite Solar Cells. *Chemsuschem* **2017**, *10*, 3687−3704.
(30) Castro, E.; Zavala, G.; Seetharaman, S.; D'Souza, F.; Echegoyen, L. Impact of Fullerene Derivative Isomeric Purity on the Performance of Inverted Planar Perovskite Solar Cells. *J. Mater. Chem. A* **2017**, *5*, 19485−19490.
(31) Li, B.; Zhen, J.; Wan, Y.; Lei, X.; Liu, Q.; Liu, Y.; Jia, L.; Wu, X.; Zeng, H.; Zhang, W.; Wang, G.-W.; Chen, M.; Yang, S. Anchoring Fullerene onto Perovskite Film via Grafting Pyridine toward Enhanced Electron Transport in High-Efficiency Solar Cells. *ACS Appl. Mater. Interfaces* **2018**, *10*, 32471−32482.
(32) Zhen, J.; Zhou, W.; Chen, M.; Li, B.; Jia, L.; Wang, M.; Yang, S. Pyridine-functionalized fullerene additive enabling coordination interactions with CH3NH3PbI3 perovskite towards highly efficient bulk heterojunction solar cells. *J. Mater. Chem. A* **2019**, *7*, 2754−2763.
(33) Castro, E.; Fernandez-Delgado, O.; Arslan, F.; Zavala, G.; Yang, T.; Seetharaman, S.; D'Souza, F.; Echegoyen, L. New thiophene-based C60 fullerene derivatives as efficient electron transporting materials for perovskite solar cells. *New J. Chem.* **2018**, *42*, 14551−14558.
(34) Pascual, J.; Delgado, J. L.; Tena-Zaera, R. Physicochemical Phenomena and Application in Solar Cells of Perovskite:Fullerene Films. *J. Phys. Chem. Lett.* **2018**, *9*, 2893−2902.
(35) He, Y.; Li, Y. Fullerene Derivative Acceptors for High Performance Polymer Solar Cells. *Phys. Chem* **2011**, *13*, 1970−1983.
(36) Hummelen, J. C.; Knight, B. W.; LePeq, F.; Wudl, F.; Yao, J.; Wilkins, C. L. Preparation and Characterization of Fulleroid and Methanofullerene Derivatives. *J. Org. Chem.* **1995**, *60*, 532−538.
(37) Tian, C.; Castro, E.; Betancourt-Solis, G.; Nan, Z.; Fernandez-Delgado, O.; Jankuru, S.; Echegoyen, L. Fullerene Derivative with a Branched Alkyl Chain Exhibits Enhanced Charge Extraction and Stability in Inverted Planar Perovskite Solar Cells. *New J. Chem.* **2018**, *42*, 2896−2902.
(38) Sun, Q.; Wang, H.; Yang, C.; Li, Y. Synthesis and Electroluminescence of Novel Copolymers Containing Crown Ether Spacers. *J. Mater. Chem.* **2003**, *13*, 800−806.
(39) Murgatroyd, P. N. Theory of Space-charge-limited Current Enhanced by Frenkel Effect. *J. Phys. D: Appl. Phys.* **1970**, *3*, 151−156.
(40) Noel, N. K.; Abate, A.; Stranks, S. D.; Parrott, E. S.; Burlakov, V. M.; Goriely, A.; Snaith, H. J. Enhanced Photoluminescence and Solar Cell Performance via Lewis Base Passivation of Organic-Inorganic Lead Halide Perovskites. *ACS Nano* **2014**, *8*, 9815−9821.
(41) Ahn, N.; Son, D.-Y.; Jang, I.-H.; Kang, S. M.; Choi, M.; Park, N.-G. Highly Reproducible Perovskite Solar Cells with Average Efficiency of 18.3% and Best Efficiency of 19.7% Fabricated via Lewis Base Adduct of Lead(II) Iodide. *J. Am. Chem. Soc.* **2015**, *137*, 8696−8699.

DOI: 10.1021/acsami.9b09018
ACS Appl. Mater. Interfaces 2019, 11, 34408−34415